Science
AAAS

Detection of Water in the LCROSS Ejecta Plume

Anthony Colaprete, *et al.*

Science **330**, 463 (2010);
DOI: 10.1126/science.1186986

This copy is for your personal, non-commercial use only.

If you wish to distribute this article to others, you can order high-quality copies for your colleagues, clients, or customers by clicking here.

Permission to republish or repurpose articles or portions of articles can be obtained by following the guidelines here.

The following resources related to this article are available online at www.sciencemag.org (this infomation is current as of May 11, 2011):

Updated information and services, including high-resolution figures, can be found in the online version of this article at:
http://www.sciencemag.org/content/330/6003/463.full.html

Supporting Online Material can be found at:
http://www.sciencemag.org/content/suppl/2010/10/21/330.6003.463.DC1.html
http://www.sciencemag.org/content/suppl/2010/10/21/330.6003.463.DC2.html

A list of selected additional articles on the Science Web sites **related to this article** can be found at:
http://www.sciencemag.org/content/330/6003/463.full.html#related

This article **cites 19 articles**, 5 of which can be accessed free:
http://www.sciencemag.org/content/330/6003/463.full.html#ref-list-1

This article has been **cited by** 6 articles hosted by HighWire Press; see:
http://www.sciencemag.org/content/330/6003/463.full.html#related-urls

This article appears in the following **subject collections:**
Planetary Science
http://www.sciencemag.org/cgi/collection/planet_sci

Downloaded from www.sciencemag.org on May 11, 2011

Science (print ISSN 0036-8075; online ISSN 1095-9203) is published weekly, except the last week in December, by the American Association for the Advancement of Science, 1200 New York Avenue NW, Washington, DC 20005. Copyright 2010 by the American Association for the Advancement of Science; all rights reserved. The title *Science* is a registered trademark of AAAS.

Detection of Water in the LCROSS Ejecta Plume

Anthony Colaprete,[1]* Peter Schultz,[2] Jennifer Heldmann,[1] Diane Wooden,[1] Mark Shirley,[1] Kimberly Ennico,[1] Brendan Hermalyn,[2] William Marshall,[1,8] Antonio Ricco,[1] Richard C. Elphic,[1] David Goldstein,[3] Dustin Summy,[3] Gwendolyn D. Bart,[4] Erik Asphaug,[5] Don Korycansky,[5] David Landis,[6] Luke Sollitt[7]

Several remote observations have indicated that water ice may be presented in permanently shadowed craters of the Moon. The Lunar Crater Observation and Sensing Satellite (LCROSS) mission was designed to provide direct evidence (*1*). On 9 October 2009, a spent Centaur rocket struck the persistently shadowed region within the lunar south pole crater Cabeus, ejecting debris, dust, and vapor. This material was observed by a second "shepherding" spacecraft, which carried nine instruments, including cameras, spectrometers, and a radiometer. Near-infrared absorbance attributed to water vapor and ice and ultraviolet emissions attributable to hydroxyl radicals support the presence of water in the debris. The maximum total water vapor and water ice within the instrument field of view was 155 ± 12 kilograms. Given the estimated total excavated mass of regolith that reached sunlight, and hence was observable, the concentration of water ice in the regolith at the LCROSS impact site is estimated to be 5.6 ± 2.9% by mass. In addition to water, spectral bands of a number of other volatile compounds were observed, including light hydrocarbons, sulfur-bearing species, and carbon dioxide.

Neutron scattering measurements by Lunar Prospector (*2*) indicated increased concentrations of hydrogen at latitudes within 20° of the poles; subsequent observations from Earth and spacecraft have provided further evidence for the presence of trace amounts of ice or bound OH on the Moon (*3*–*5*). Neither the chemical form of the hydrogen-bearing compounds nor their origins has been determined; a variety of studies have postulated sources, including solar wind, asteroids, and comets (*6*–*10*). Clementine radar observations showed a bright radar return from the interior of Shackleton Crater consistent with volumetric scattering by water ice (*11*), a process requiring this ice to be relatively pure (~90%) and 1 to 2 m thick. The goal of the Lunar Crater Observation and Sensing Satellite (LCROSS) was to provide ground truth at one location—the crater Cabeus—for these observations by crashing a spent rocket stage into the Moon and observing the ejected debris, including any hydrogen species, from instruments on a trailing spacecraft.

The impactor was the spent upper stage of the Atlas V rocket, the Centaur, which propelled both the Lunar Reconnaissance Orbiter (LRO) and LCROSS to the Moon. Shortly after launch, LRO separated from the LCROSS-Centaur stack, the Centaur vented its remaining fuel, and control was assumed by the LCROSS Shepherding Spacecraft (SSc). The LCROSS SSc then controlled the Centaur for the next 4 months, performing maneuvers to allow the sun to bake out residual water (*12*), perform instrument calibrations, and ultimately target the Centaur at the planned impact site. Approximately 9 hours before impact, the SSc separated from the Centaur, performed a braking burn to build a 4-min separation between itself and the Centaur at impact, and oriented its instruments in the direction of the targeted impact site. About 1 hour before impact, the nine LCROSS instruments were powered on and began taking data (*13*). Observations from the near-infrared (NIR) and ultraviolet/visible (UV/Vis) spectrometers are described here [(*14*) and supporting online material (SOM)].

The LCROSS target site was selected using a variety of criteria; the two most important were the altitude at which ejecta would be illuminated by sunlight and evidence of elevated levels of hydrogen from previous measurements. Topographic data and its orientation to the Sun indicated that Cabeus was the most compelling target (*15*–*18*). Substantial levels of hydrogen were indicated in Cabeus by both the Lunar Prospector Neutron Spectrometer (LPNS) and the Lunar Exploration Neutron Detector (LEND) (*2*, *18*). The height required for the debris to reach sunlight was 833 m at the Centaur impact site and time, based on the comparatively low latitude of Cabeus (~–81.5°S) and a cleft in the crater rim topography on the sunward side at the time of impact. This observation geometry also provided a dark background for the nadir spectrometer measurements. The area selected for impact showed temperatures less than 50 K (*19*), making it a likely cold trap for volatiles.

Immediately after the impact [see (*20*) for details], a hot (1000 K) vapor cloud emerged from the crater, followed by low- and high-angle (relative to the surface) ejecta. The two spectrometers measured both thermal emission from the hot (~300 to 1000 K) ejecta (derived from a fit of the NIR spectrometer spectra and consistent with LRO and Diviner Lunar Radiometer measurements) and solar scattering from sunlit debris (both NIR and UV/Vis spectrometers). The debris cloud reached sunlight about 1 s after impact, and peak brightness in UV/Vis spectra was approximately 17 s after impact. Brightness waned to a persistent level substantially above preimpact background for another 223 s thereafter (Fig. 1). The total radiance time profile from the NIR spectrometer was unlike that from a simply dissipating scattering dust source: Radiance jumped well above background just after impact, but the total radiance continued to rise during the next 180 s. The lower initial total radiance measured by the NIR spectrometer (one-fifth that of the UV/Vis radiance) is attributed to two factors. First, the ejecta cloud did not efficiently scatter NIR; models suggested a ratio of UV/Vis-to-NIR of 2.5, but the observed ratio was 5, indicating grains smaller than a few microns. Second, a high concentration of dust or species that absorbed

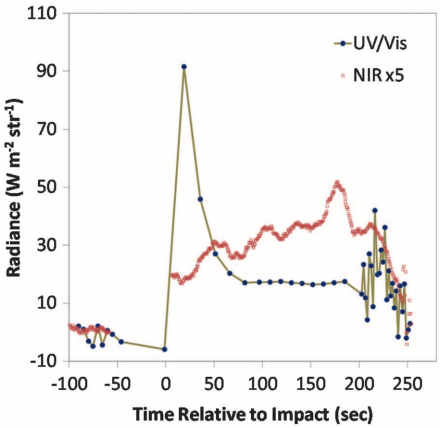

Fig. 1. The total ejecta cloud radiance (summed across sampled wavelength space) measured by the NIR and UV/Vis spectrometers as a function of time relative to impact. The total radiance for the ejecta cloud alone was derived by subtracting from the total measurement of radiance a fit to scattered light and light from illuminated surfaces in the instruments' FOVs. For clarity, the NIR radiance has been multiplied by a factor of 5. The gap in the NIR data ~1 min before impact corresponds to when the nadir NIR spectrometer was placed into "flash" mode, a mode in which only five spectral positions are sampled but are done so at about 72 Hz. These data are not used in the analysis presented here. Also, the reconfiguration of the UV/Vis spectrometer for long integration times results in a sampling pause just before impact.

[1]NASA Ames Research Center, Moffett Field, CA 94035, USA. [2]Brown University, Providence, RI 02912, USA. [3]University of Texas at Austin, Austin, TX 78712, USA. [4]University of Idaho, Moscow, ID 83844, USA. [5]University of California Santa Cruz, Santa Cruz, CA 95064, USA. [6]Aurora Design and Technology, Palm Harbor, FL 34685, USA. [7]The Citadel, Charleston, SC 29409, USA. [8]Universities Space Research Association, Mountain View, CA 94043, USA.

*To whom correspondence should be addressed. E-mail: Anthony.Colaprete-1@nasa.gov

Downloaded from www.sciencemag.org on May 11, 2011

in the NIR (described below) lowered integrated radiance across most of the NIR spectrum, an effect also seen both experimentally and in the Deep Impact mission (*21*). After the impact, the abundance of NIR absorbers diminished as the plume expanded kinetically and departed the field of view (FOV) of the instrument. However, in general, at wavelengths longer than about 1.9 μm, the radiance increased as range decreased between the instrument and the warm, emitting crater (Fig. 2).

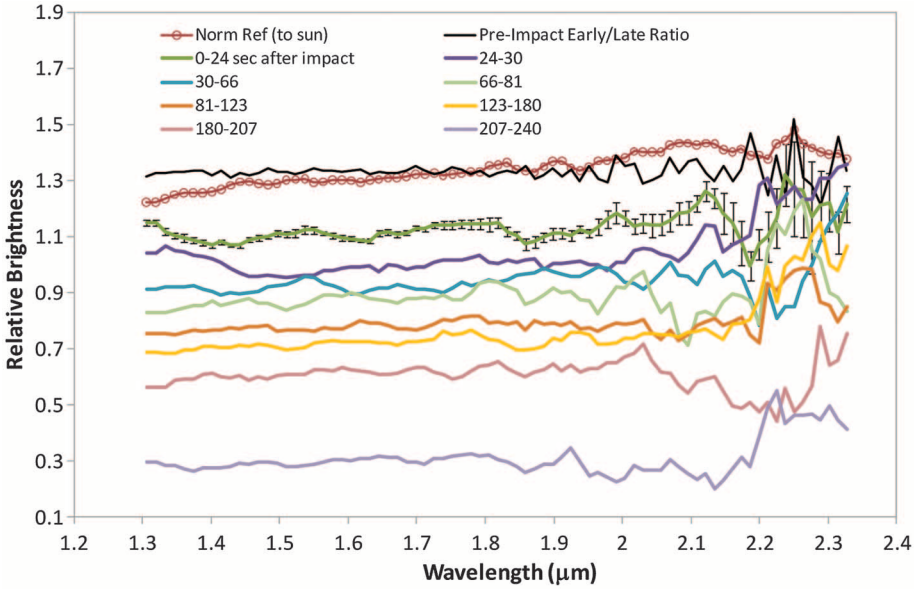

Fig. 2. Scaled reflectance NIR spectra for different time periods relative to impact, with each spectrum offset vertically in brightness for clarity. Each spectrum is an average over the time period indicated in the figure key (50 s is ~83 spectra) and is smoothed over 5 spectral bins (~0.07 μm). Also shown is a preimpact reference spectrum [divided by the solar radiance convolved to the instrument resolution (*14*) and normalized], constructed from an average of 180 scans taken ~30 min before impact, as well as the ratio of the first 90 of these scans (Pre-Impact Early) and the second 90 of these scans (Pre-Impact Late). The spectra measured after impact were divided by a preimpact reference spectrum that was generated from spectra taken during the last 90 s just before impact, to derive the relative reflectance spectra of the ejecta cloud. ±1 SD error bars are shown for reference on one of the postimpact spectra.

The nadir NIR spectrometer measurements after impact were dynamic, with significant variations across the measured spectrum as a function of time (Fig. 2). We used 180 measurements taken in the ~90 s before impact to generate a reference spectrum against which postimpact spectra could be compared. After impact, various time series of scans were averaged to improve signal-to-noise ratios. Each NIR spectrometer scan took ~0.6 s; thus, averaging across 30 scans effectively averages over ~20 s. The averaging time period was guided by discernible periods of distinct NIR phenomenology, as indicated by the peaks and valleys in the total NIR radiance (Fig. 1). These differentiable periods are likely to be the result of changes in the FOV of the instrument (during descent toward the impact site) (*22*), and changes in the morphology of the ejecta and vapor clouds, as debris moved into sunlight and volatiles continued to sublimate from ejecta grains and the warmed surfaces in and around the impact crater. During the earliest periods after impact, there was a clear indication of a NIR contribution from scattered solar light (see Fig. 2, spectra for periods 0 to 24 and 24 to 30 s). This contribution is seen as an upturn at wavelengths shorter than ~1.5 μm. At longer wavelengths, the continuum is composed of a combination of weak scattering from ejecta debris and the surface, and emission from the hot crater (*23*). Over all spectral periods, the continuum generally appeared to be heavily eroded by a variety of absorbers. After about 30 s, gas absorption bands, which were

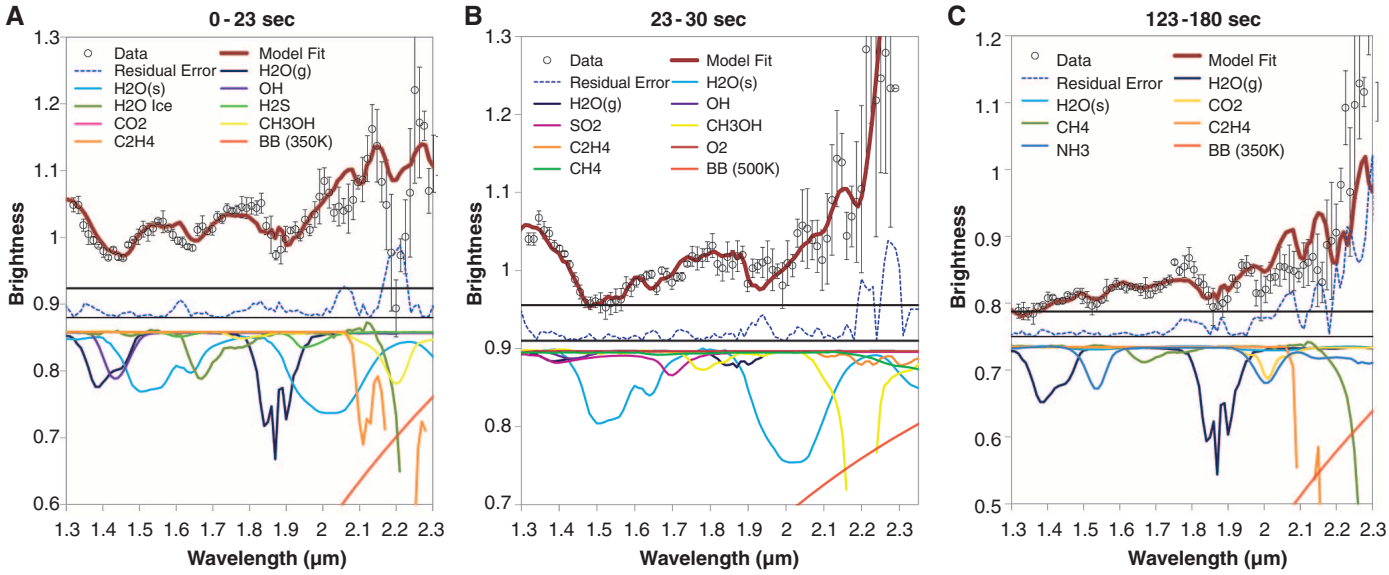

Fig. 3. (**A** to **C**) Model fits to the NIR reflectance spectra for three periods after impact. The measured spectral reflectance is shown with 1 SD error bars (measurement variance for the average of ~90 spectra). The fit ("Model Fit") was produced using the various volatiles indicated by the curves (each curve is normalized to water ice to show relative abundances with respect to each other) at the lower part of each figure [H_2O(g) and H_2O(s) are water vapor and water ice, respectively]. Water vapor fluorescent emission is provided as a possible contribution but is not found to be necessary to fit the data within the uncertainty of the measurements. The total residual error between the observation and the model is shown (dark blue dashed line) and the 5% level indicated by a solid black line. In the wavelength range between 1.3 and 2.0 μm, residual error is typically <1.5%. The χ^2/ν for each of the three fits is 1.16, 1.8, and 1.2, respectively.

Downloaded from www.sciencemag.org on May 11, 2011

narrower than mineral absorption bands, dominated the spectra. We used a linear mixing model to fit the spectra, and the quality of fit was determined by the total residual between the measurements and the fit from 1.3 to 2.0 μm—the region where water vapor and ice are primarily involved. A χ^2 minimization was performed for three epochs to elucidate the uncertainties with respect to their related confidence intervals (*24*). Linear fits for three of the periods shown in Fig. 2 are shown in Fig. 3. The model fit is good at wavelengths <2.0 μm, where residual errors are typically less than 1.5%. At longer wavelengths, where the instrument performance is poorest and the variance from one spectrum to the next is greatest due in part to variations in the blackbody source function, the fit is not as good. Moreover, because the NIR source function was not dominated by scattering from ejecta debris, especially over 30 to 40 s after impact, narrow gas lines were evident in the spectra and could be used to derive abundances of gaseous species. Thus, the fitting of the water features at wavelengths <2 μm did not depend strongly on the fitting of species that absorb at wavelengths >2 μm.

In Fig. 3A, there is a strong indication of absorption by hydroxyl (OH) and water (vapor and possibly mineral bound). It is likely that OH and water gasses were part of an initial warm (~1000 K) vapor plume that was released just after impact and that is generally unassociated with ejecta debris–sunlight interaction. The combination of features seen at 1.4, 1.9, and 2.2 μm suggest that mineral-bound OH (at 1.4 μm), bound H_2O (at 1.9 μm), and metal-bound OH (e.g., Al-OH at 2.2 μm feature) were also present (*26*) but in substantially smaller quantities than gas-phase water. Figure 3B shows spectra from the period when the ejecta cloud was brightest and provides the greatest shortwave contrast for the water ice feature at 1.5 μm. This ice feature and its 2.0-μm counterpart (which is skewed to higher reflectance because of the thermal emission beginning at 1.9 μm) confirm that at least some of the water ejected from Cabeus was in the form of ice and not just water adsorbed on grains. At later times, the water vapor feature at 1.87 μm again became apparent (Fig. 3C) and persisted for the remaining duration of the 4-min observation period (compare spectra at 1.87 μm in Fig. 2).

Using the depth of the 1.87-μm absorption band in the spectrum in Fig. 3C and absorption cross sections computed using high-resolution transmission molecular absorption database (HITRAN), the total water vapor in the instrument FOV at the time of the observation was ~5.1 (±1.4) × 10^{19} molecules m^{-2} (1 SD uncertainty) (*24*). Over the period of the observation (123 to 180 s), the FOV of the spectrometer ranged from ~3.8 × 10^7 to 2 × 10^7 m^2, giving a total water vapor mass in the instrument FOV ranging from 74 to 31 kg. Given the average FOV over this period, the water vapor mass is 53 ± 3 kg (1 SD uncertainty). Similarly, the total water ice abundance over this same period ranged from 22 to 9 kg, with an average in that time period of 16 ± 2 kg (1 SD uncertainty) (*27*). These are lower limits, because the ejecta cloud filled the spectrometer FOV ~20 s after impact, and thus some water would be outside the instrument's FOV. In a similar manner, total water vapor columns were calculated at earlier times (Fig. 3, A and B). Using the 1.5-μm ice feature shown in Fig. 3B, we estimate using a 2-μm ice particle radius (*28*) that the water ice grain column number is 6.3 × 10^7 particles m^{-2} or ~131 ± 8 kg of water ice (Table 1).

The spectra evolution (Fig. 2) suggests that there was an initial release of vapors, including water vapor and OH, and small amounts of ice-rich ejecta that quickly (within ~20 s) passed out of the instrument FOV. This initial plume was then followed by the emergence of water ice grains that continued to sublime for the entire 4-min period of observations and possibly continued sublimation from the heated surface near the impact site. This interpretation is supported by the consistent increase in the 1.86-μm water vapor absorbance after impact (Fig. 4).

The other line of evidence for water is the detection of emission associated with hydroxyl radical (OH). Hydroxyl radical may be produced through the photodissociation of water vapor or desorption of OH from grains. OH emits near 0.308 to 0.310 μm either due to excitation concomitant with photodissociation (prompt emission), or through fluorescent scattering (*30*) [see SOM]. The OH feature is evident in the ratio of postimpact scans to a preimpact reference composed of the average of the last four UV/Vis scans just before impact (Fig. 5). We calculated the strength of the emission line at 0.3093 μm for each postimpact ratio (from Fig. 5); the local continuum was calculated as the local average between 0.304 and 0.314 μm (Fig. 6). Before impact, there was no OH band, within measurement uncertainty. The band strength increased to an initial peak about 30 s after impact. This rise time and peak are consistent with either photo-dissociative OH production in an expanding water vapor cloud with a temperature of about 1000 K (*31*) or the fluorescence of OH released at impact. The position and shape of the feature are more consistent with resonant fluorescence (*30*) (see SOM). This is also the same time period when OH absorption is evident in the NIR spectra (Fig. 3A). It is likely that the initial high-impact temperature (~1000 K) desorbed some OH from grain surfaces (*3–5*). However, if this expanding vapor cloud were the only source of OH, a rapid decline in OH emission would be expected at times longer than 30 s (*32*). Continued high levels of OH emission after 30 s and, in particular, the apparent rise after ~120 s suggests that additional sources of water vapor and possibly OH were present then. In particular, the position and shape of the OH emission after ~190 s is consistent with prompt emission (see SOM). This is also the period when NIR spectra show persistent water vapor (Figs. 2 and 3C). The LCROSS impact event resulted in a high-angle debris plume (*20*, *32*). The persistent cloud of sunlit material allowed sustained production of water vapor (from subliming water ice) and OH (from photodissociation of water vapor).

We estimated the total OH column number, using the maximum strength of the band at impact +180 s (as this OH is most likely due to water photodissociation), as approximately 8.0 × 10^{-3} W m^{-2} μm^{-1} str^{-1}, or 2.2 × 10^{16} molecules m^{-2} (*33*) corresponding to 23 ± 11 kg of water vapor (*34*). This estimate for total water vapor column from OH prompt emission strength is consistent with water vapor values derived from the NIR spectrometer for about the same time period.

The total debris mass in sunlight was estimated using UV/Vis spectrometer observations

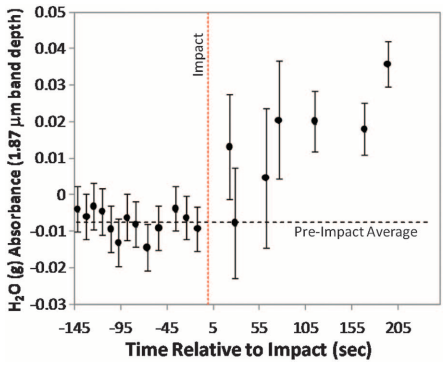

Fig. 4. The depth of the 1.87-μm water vapor band compared with the 1.77-μm shoulder in units of absorbance. Before impact, the band absorbance was calculated from averages of 30 scans. After impact, the absorbance was calculated for each of the spectra shown in Fig. 2. Also shown for reference is the approximate time of impact and the preimpact average 1.87-μm absorbance. The error bars are the root mean square of the error in radiance for each position (shoulder and band center) in the spectrum.

Table 1. Summary of the total water vapor and ice and ejecta dust in the NIR instrument FOV. Values shown are the average value across the averaging period, and errors are 1 SD.

	Water mass (kg)			
Time (s)	Gas	Ice	Dust mass (kg)	Total water %
0–23	82.4 ± 25	58.5 ± 8.2	3148 ± 787	4.5 ± 1.4
23–30	24.5 ± 8.1	131 ± 8.3	2434 ± 609	6.4 ± 1.7
123–180	52.5 ± 2.6	15.8 ± 2.2	942.5 ± 236	7.2 ± 1.9
Average	53 ± 15	68 ± 10	2175 ± 544	5.6 ± 2.9

Downloaded from www.sciencemag.org on May 11, 2011

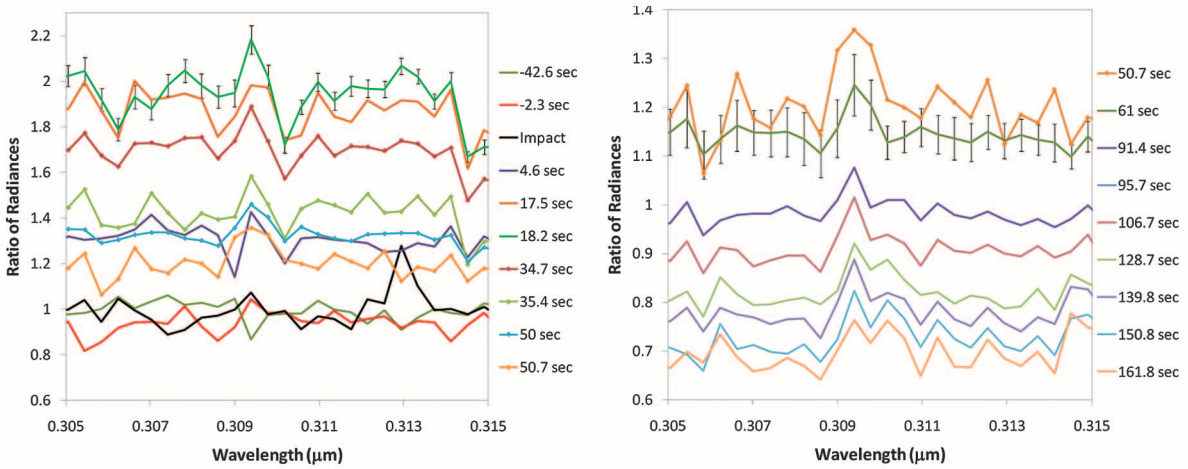

Fig. 5. Ratio of postimpact UV/Vis spectra to a preimpact UV/Vis reference spectrum for several times just before and after impact. Spectra at individual times are distributed across three panels for clarity. Error bars (derived from instrument dark measurements) are shown on a single spectrum in each panel for reference. The gradual increase and then decrease in the overall ratio level from impact through about impact +160 s is the result of the brightening and then dimming of the ejecta cloud. The emission resulting from OH is apparent between 0.3085 μm and 0.3095 μm. The shape of the OH emission is consistent with fluorescence at early times and with prompt emission at late times (see SOM).

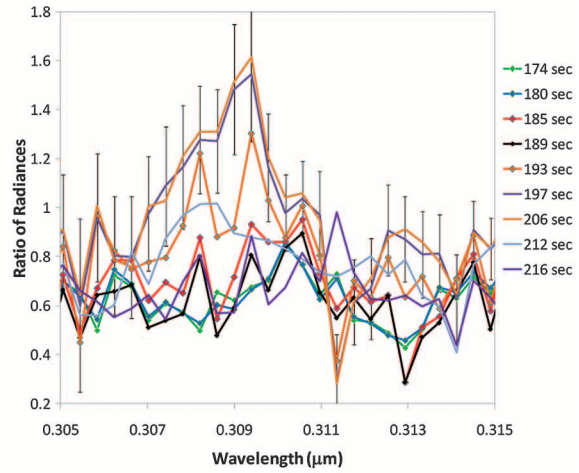

of the ejecta cloud brightness as a function of wavelength. This quantity permits us to relate the total water seen in the instrument's FOVs to the concentration of water in the regolith. These data were fit using a radiative transfer model (*27*). Using the highest levels of radiance from the cloud measured shortly after impact (before ~30 s after impact) (Fig. 1) and a fit using an area-weighted grain radius of 2.5 μm results in a visible ($\lambda = 0.5$ μm) optical depth of 0.002 to 0.003. For a uniform distribution along the line of sight, these values for the optical depth imply a number density of approximately 1.4×10^6 to 2.1×10^6 grains m^{-2}. Based on visible camera images, the ejecta cloud filled about half the spectrometer FOV at 8 s and the entire FOV at 20 s. A uniform distribution of ejecta debris across the instrument FOV results in a total ejecta cloud mass in sunlight of ~4300 to 6500 kg for the range of debris column densities. If an average area filling factor of 58% (*35*) is applied to account for FOV underfilling before 20 s, the total mass is approximately 2500 kg and 3800 kg for the low and high estimates, respectively, with an average mass of 3150 ± 790 kg. At times later than 30 s after impact, the total cloud brightness dropped by a factor of ~3.2 (Fig. 1) and remained fairly constant for another ~200 s. During this period, the cloud optical depth was ~9.3×10^{-4} (for a linear scaling with measured brightness), corresponding to a cloud mass of 1850 kg. This estimate of optical depth is consistent with the optical depth derived by LRO Diviner observations for the period ~90 s after impact (*23*). Using the estimates of the ejecta cloud mass and water from just after impact estimated for the instrument FOVs at the beginning and end of the averaging period (0 to 23 s, with the FOV filling factor applied), the total water mixing ratio in the ejecta cloud was between 4.1 and 5.1% by mass, with an average over the period of 4.5 ± 1.4% (Table 1). It is difficult to differentiate water vapor that sublimated from water ice grains in sunlight from water vapor sublimated from heated surfaces in and near the crater; thus, these estimates for the total mixing ratio of water in the ejecta cloud, based on the mass of ejecta observed in sunlight, are likely to be overestimates during this early period when the ejecta cloud was smaller than the instrument FOV. If only water ice as derived from the 23- to 30-s period (135 kg on average) and the estimates for the total ejecta cloud mass in the instrument FOV are used, the range of mixing ratios of ice in the ejecta cloud over this period was 5.2 to 5.5% by mass, with an average of 5.4 ± 1.4% by mass. Using all deri-

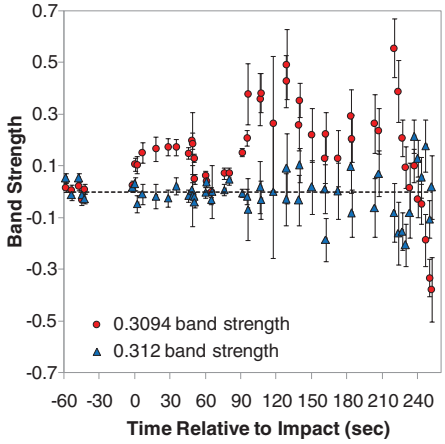

Fig. 6. Calculated band strength at 0.3094 μm (OH emission) and 0.312 μm (nearby off-band wavelength for comparison) as a function of time relative to impact. The error bars show the ±1 SD variance across the continuum used to calculate the band depth. The 0.3094-μm band shows a clear rise in strength just after impact that remains above the preimpact baseline (dashed line) for the remaining 4-min observation duration, while the off-band measurement at 0.312 μm stays at the baseline (within error estimates).

Downloaded from www.sciencemag.org on May 11, 2011

Table 2. Abundances derived from spectral fits shown in Fig. 3. The uncertainty in each derived abundance is shown in parenthesis [e.g., for H_2O: 5.1(1.4)E19 = 5.1 ± 1.4 × 10^{19} cm^{-2}] and was derived from the residual error in the fit and the uncertainty in the radiance at the appropriate band center.

Compound	Molecules cm^{-2}	% Relative to $H_2O(g)$*
H_2O	5.1(1.4)E19	100.00%
H_2S	8.5(0.9)E18	16.75%
NH_3	3.1(1.5)E18	6.03%
SO_2	1.6(0.4)E18	3.19%
C_2H_4	1.6(1.7)E18	3.12%
CO_2	1.1(1.0)E18	2.17%
CH_3OH	7.8(42)E17	1.55%
CH_4	3.3(3.0)E17	0.65%
OH	1.7(0.4)E16	0.03%

*Abundance as described in text for fit in Fig. 3C.

vations of total water concentration and the errors from individual measurements for each of the three periods shown in Fig. 3, the mean water concentration is 5.6 ± 2.9% by mass (*36*). These high values suggest that a substantial amount of the hydrogen observed by LPNS and LEND was in the form of water ice in the crater. LEND neutron data suggests that the floor of Cabeus contains >2 weight percent water (*18*), or about a third the value derived from LCROSS. Several important caveats need to be considered: (i) the LEND result is strongly model dependent (e.g., assumptions about the desiccated top layer thickness); (ii) the LCROSS sample depth was possibly deeper than neutron spectroscopy can effectively sample (deeper than ~0.7 m); (iii) the persistent conduction of impact heat into the regolith resulted in a continued release of volatiles (*23*); and (iv) the neutron LEND and LPNS instrument footprints were never smaller than 10 km across; thus, spatial gradients smaller than 10 km are smoothed. The LCROSS result when combined with LEND and LPNS suggests that there is some spatial heterogeneity at scales <10 km.

As implied in Fig. 3, other hydrogen-bearing compounds are also likely to be present. Observations from the Lyman Alpha Mapping Project (LAMP) on LRO suggest that ~140 kg of H_2 was released at impact, corresponding to an initial regolith concentration of 1.4% (*31*). The total hydrogen sensed by LPNS and LRO LEND would logically include not only the water measured by LCROSS's spectrometers but also H_2 measured by LRO-LAMP and any other hydrogen-containing volatiles (e.g., CH_4) measured by LCROSS.

The abundances of volatile species other than water vapor were also derived using HITRAN [local thermal equilibrium (LTE) at room temperature, 1 atm] cross sections convolved to the instrument resolution. Given the caveat that the LCROSS impact plume contained low-density and rapidly cooling gases, probably far from equilibrium, the abundances are derived and given (Table 2). Of interest is the indication from this preliminary analyses that some volatiles other than water are considerably more abundant (some by orders of magnitude) than the ratios found in comets, in the interstellar medium, or predicted from gas-gas reactions in the protoplanetary disk (*37*). Rather, the H_2S/H_2O, NH_3/H_2O, SO_2/H_2O, and CO/H_2O (*31*) are more commensurate with the abundances of those molecules in molecular hot cores (*38*). In hot cores, gas-phase abundances are enhanced by the release of molecules that have formed on cold grain surfaces in previous stages of the prenatal cloud. In the persistently shadowed region (PSR) of Cabeus, molecule formation on cold grain surfaces could enhance abundances compared with water. One can infer that the reservoir of volatiles that LCROSS struck may partly have cometary and/or asteroidal origins but probably also has volatile molecules that may have formed in situ on cold grain surfaces in the PSR. Molecules forming on grain surfaces in cold, dense molecular clouds occur primarily through neutral-neutral reactions because the gas is very weakly ionized by cosmic rays that penetrate deep into the cloud. Conversely, the solar wind and plasma environment of the lunar exosphere is expected to have some charged species.

References and Notes

1. A. Colaprete *et al.*, Abstract 1861, *40th Lunar and Planetary Science Conference* (Lunar and Planetary Science XL, Houston, TX, 2009).
2. W. C. Feldman *et al.*, *Science* **281**, 1496 (1998).
3. C. M. Pieters *et al.*, *Science* **326**, 568 (2009).
4. R. N. Clark, *Science* **326**, 562 (2009).
5. J. M. Sunshine *et al.*, *Science* **326**, 565 (2009).
6. K. Watson, B. C. Murray, H. Brown, *J. Geophys. Res.* **66**, 3033 (1961).
7. J. R. Arnold, *J. Geophys. Res.* **84** (B10), 5659 (1979).
8. R. R. Hodges Jr., *Lunar Planet. Sci.* **12**, 451 (1981).
9. R. C. Elphic, V. R. Eke, L. F. A. Teodoro, D. J. Lawrence, D. B. J. Bussey, *Geophys. Res. Let.* **13**, L13204 (2007).
10. D. H. Crider, R. R. Vondrak, *J. Geophys. Res.* **105** (E11), 26,773 (2003).
11. P. D. Spudis *et al.*, *Sol. Syst. Res.* **32**, 17 (1998).
12. The residual H_2, O_2, and H_2O on the Centaur at the time of impact were <0.5, <1.25, and <1.5 kg, respectively. See SOM for additional description of in-flight measurement contamination control activities.
13. K. Ennico *et al.*, Abstract 1878, *40th Lunar and Planetary Science Conference* (Lunar and Planetary Science XL, Houston, TX, 2009).
14. The instrument suite included two down (nadir) viewing spectrometers both with a coaligned 1° FOV. The nadir NIR spectrometer measured wavelengths between 1.25 and 2.35 μm with a resolving power between 35 and 70. The UV/Vis spectrometer measured wavelengths between 0.26 and 0.65 μm, with a resolving power between 300 and 850. Additional information is provided in the SOM.
15. H. Noda *et al.*, *Geophys. Res. Lett.* **35**, L24203 (2008).
16. T. P. McClanahan *et al.*, Abstract 2092, *40th Lunar and Planetary Science Conference* (Lunar and Planetary Science XL, Houston, TX, 2009).
17. L. F. A. Teodoro *et al.*, abstr. 1515, *Annual Meeting of the Lunar Exploration Analysis Group* (Houston, TX, 2009).
18. I. G. Mitrofanov *et al.*, *Science* **330**, 483 (2010).
19. D. A. Paige *et al.*, *Science* **330**, 479 (2010).
20. P. H. Schultz *et al.*, *Science* **330**, 468 (2010).
21. P. H. Schultz *et al.*, *Icarus* **190**, 295 (2007).
22. The observations spacecraft, the SSc, was three-axis stabilized and pointed to the impact target to within ±0.1 deg.
23. P. O. Hayne *et al.*, *Science* **330**, 477 (2010).
24. The best fit for the temporal sampling of 80 to 123 s (Fig. 3C) corresponds to a goodness-of-fit value of χ^2/ν = 1.19 for the number of free parameters (ν) equal to the number of points (75) minus the number of parameters (*9*). The nine parameters are the IR continuum and the eight scalers for the molecular absorbance of the species shown in Fig. 3C. For confidence levels of 68% (1 SD), 95% (2 SD), and 99.7% (3 SD), the independent point errors on the water vapor are (+5,–5) %, (+7,–10) % and (+12,–24) %, determined for the parameters values for which $\chi^2/\nu = \chi^2/\nu(\min) + \Delta\chi^2(9\ \text{parameters})/\nu$ (*25*). An error of ±25% in the scaler of the molecular absorbance corresponds to better than 99% confidence or better than 3 SD. The fractional error in the corresponding water vapor column density is then the root mean square of the independent point error in the linear mixing model (±5% at 1 SD) and the uncertainty in the radiance measurement at the 1.87-μm band center (~28% in the spectrum in Fig. 3C). Thus, the water vapor mass is uncertain to ±28% (1 SD).
25. W. H. Press *et al.*, *Numerical Recipes* (Cambridge Univ. Press, New York, 2007), chap. 15.
26. R. N. Clark, T. V. V. King, M. Klejwa, G. A. Swayze, N. Vergo, *J. Geophys. Res.* **95** (B8), 12653 (1990).
27. The UV/Vis and NIR spectrometer ejecta cloud radiance was modeled using the multistream radiative transfer model DISORT with the appropriate incident and observation viewing angles. The ejecta cloud grain optical properties were calculated using Mie theory and a log-normal distribution of particles with a range of area weighted mean radii between 1 and 35 μm, a variance of 1.5, and indices of refraction for silicon dioxide. The mixed ice-dust cloud optical properties were approximated using a linear mix of pure water ice and pure silicon dioxide grains. The model used to calculate the amount of water ice assumes a scattering layer of dust (ejecta) mixed with water ice. The model is multistream, with the ejecta cloud approximated as five layers with the top layer and bottom layers being ice free (although, due to the low optical depths, the result is mostly insensitive to the arrangement of ice in these layers). A grain density of 3000 kg m^{-3} was assumed when calculating the total cloud mass. The NIR water ice column optical depth was modeled in the same way. The 1.5-μm feature could be modeled to within about 14% (root mean square of 11% from fitting uncertainty and 9% from radiance measurement uncertainty). Using a 2.5-μm particle, consistent with observed UV/Vis-to-NIR radiance ratio, the UV/Vis continuum was fit with an uncertainty in the optical depth of ~25% (5% from fitting uncertainty and 24% in radiance measurement uncertainty).
28. The water ice grain radius is estimated based on the band position in the spectrum shown in Fig. 3B. Submicron ice grains will have a band center less than 1.48 μm, and for a 15+ μm grain radius the band center is ~1.54 μm (*29*). The 1.5-μm band center is at ~1.51 μm, which is consistent with an ice grain ~2 μm.
29. J. E. Hansen, J. B. Pollack, *J. Atmos. Sci.* **27**, 265 (1970).
30. P. Rousselot *et al.*, *Asteorids, Comets, Meteors* (Lunar and Planetary Institute, Houston, TX, 1991).
31. G. R. Gladstone *et al.*, *Science* **330**, 472 (2010).

Downloaded from www.sciencemag.org on May 11, 2011

32. D. Summy *et al.*, abstr. 2267, *40th Lunar and Planetary Science Conference*, (Lunar and Planetary Science XL, Houston, TX, 2009).
33. A g factor of 5×10^{-4} photons/s was used in the OH number estimate.
34. The uncertainty in the water vapor mass derived from the OH prompt emission at ~180 s after impact is based on the total uncertainty in the measured OH radiance at that time. The total uncertainty in OH radiance is based on the calibration error (<10%), instrument noise (from dark measurements at specific integration time), and uncertainty in the g factor (about 20%).
35. At 8 s after impact, the diameter of the ejecta cloud in the visible camera was ~4.5 km, and the FOVs of the NIR and UV/Vis spectrometers were ~10 km in diameter. At 20 s, the ejecta cloud diameter was ~8.5 km and the FOVs of the spectrometers were approximately 9.6 km in diameter.
36. The total error is the propagated error for the masses of water vapor plus water ice divided by the dust mass, using the errors (1 SD uncertainties, quoted in Table 1) in the derived masses of each component.
37. D. Bockele'e-Morvan *et al.*, in *Comets II* (University of Arizona Press, Tucson, AZ, 2004), pp. 391–423.
38. D. H. Wooden *et al.*, in *Comets II* (University of Arizona Press, Tucson, AZ, 2004), pp. 33–66.
39. We thank the LCROSS Project and NASA's Exploration Systems Mission Directorate (ESMD) and NASA Science Mission Directorate (SMD) for support, and are very grateful to the LRO project and the LRO instrument leads for supporting the LCROSS targeting and impact observations, and for the three referees who provided reviews that greatly improved this paper. R.C.E. was supported by an LRO Participating Scientist grant.

Supporting Online Material
www.sciencemag.org/cgi/content/full/330/6003/463/DC1
SOM Text
Figs. S1 to S11
References

12 January 2010; accepted 22 September 2010
10.1126/science.1186986

REPORTS

The LCROSS Cratering Experiment

Peter H. Schultz,[1]* Brendan Hermalyn,[1] Anthony Colaprete,[2] Kimberly Ennico,[2] Mark Shirley,[2] William S. Marshall[2,3]

As its detached upper-stage launch vehicle collided with the surface, instruments on the trailing Lunar Crater Observation and Sensing Satellite (LCROSS) Shepherding Spacecraft monitored the impact and ejecta. The faint impact flash in visible wavelengths and thermal signature imaged in the mid-infrared together indicate a low-density surface layer. The evolving spectra reveal not only OH within sunlit ejecta but also other volatile species. As the Shepherding Spacecraft approached the surface, it imaged a 25- to-30-meter–diameter crater and evidence of a high-angle ballistic ejecta plume still in the process of returning to the surface—an evolution attributed to the nature of the impactor.

Prior studies from instruments on the Apollo (*1*) and Lunar Prospector (*2*) missions indicated the presence of mobile volatiles on or around the Moon. Multiple spacecraft recently confirmed these observations through direct spectroscopic measurements of OH and H_2O (*3*–*5*). In contrast, the Lunar Crater Observation and Sensing Satellite (LCROSS) mission used a kinetic probe (the emptied stage of the Centaur rocket) to excavate H-bearing compounds from a permanently shadowed region (PSR) near the south pole of the Moon. As the Centaur collided with the lunar surface, the trailing Shepherding Spacecraft (SSc) measured the evolution and composition of the resulting ejecta with a series of instruments. A separate contribution specifically examines H-bearing molecular species observed with LCROSS instruments (*6*). Here, we describe the Centaur collision with implications for the ejected mass, excavation depth, and regolith composition.

The mid-infrared cameras (MIR1 and MIR2) recorded the "first light" in the frame coinciding with the moment of impact that remained visible for the next 10 s (Fig. 1A). At that time, the resolution of the MIR instrument was approximately 1 km/pixel. Consequently, the thermal radiance generated just by the heated crater floor should have covered less than a single pixel at that range; instead, it spanned multiple pixels corresponding to 3 to 4 km in diameter before fading with time.

The Total Luminance Photometer (TLP) was designed to detect a sudden change in brightness over visible wavelengths from a distance of more than 600 km (*7*), but this signal has not yet been unequivocally identified. Nevertheless, the Near-Infrared Spectrometer (NSP1), covering longer wavelengths, operated in a flash mode at 72 Hz (five wavelength channels plus a dark measurement measured every 13.8 ms); hence, it functioned as a thermal flash detector (Fig. 1B). This instrument recorded a 0.4-s rise in background intensity, followed by a 0.7-s decay. The onset for the rise in radiance in the NSP1, however, was delayed about 0.3 s from the moment of impact, on the basis of our analysis of flight data for the trajectory and topography.

The UV/VIS Spectrometer (VSP) captured both emissions from the impact flash and ejecta rising into sunlight. A large number of weak [but significant (2σ)] emission lines emerged within the first 0.8 s after impact, during the flash mode of the NSP1 instrument. The spectral resolution of the VSP is better than 1 nm, as demonstrated through clear identification of fine structure in the solar spectrum due to scattered light. Although many emission lines have not yet been identified with confidence, possible identifications include CN, NH, NH_2, CO_2^+, and CS (*8*). The overall radiance levels increased dramatically during the next exposure (1.1 to 3.1 s after impact), indicating the arrival of ejecta into sunlight. Prominent emissions at 598 nm (Na) and a line pair at 328 and 338 nm (possibly Ag) also emerged, along with other species, such as H_2S and H_2O^+.

The Visible Camera (VIS) started its sequence ~8 s after impact, well after ejecta had reached sunlight (Fig. 2A). The ejecta cloud increased from ~4 km (8 s) to ~8 km (20 s) in diameter and remained visible for about 42 s before dropping below the sensitivity threshold of the instrument (Fig. 2B). Both near-infrared cameras (NIR1 and NIR2) also captured the expanding ejecta cloud well after (~8 s) the moment of impact but with less dynamic range than the visible camera, thereby limiting their use for comparing dimensions.

In the final 10 s before impact, changes in exposure time and pixel gain for the NIR2 camera allowed the lunar surface to be imaged from scattered light off nearby relief. As a result, "shadowed" and "illuminated" areas are opposite to the direction of direct solar illumination (Fig. 3A). These images (higher in spatial resolution than the MIR images) reveal a region around the point of impact that is typical of the lunar surface: an undulating but relatively flat surface with few large craters. The last three frames from NIR2, starting at a range of 11 km above the surface, included a feature that correlates with a small thermally warm region in the MIR. This region is identified as the crater through correlation produced by the Centaur impact and its surrounding ejecta through correlation of telemetry and registration with the hot spot located in the MIR data. Just before the SSc collision, the NIR2 camera also recorded a diffuse disk-like feature that moved through the field of view in four successive images during approach (Fig. 3B). This feature appeared suddenly as a result of the camera exposure and gain settings.

The evolving ejecta cloud and final crater produced by the Centaur impact place constraints on the nature of the surface, the depth of any released volatiles, and context for observations by other instruments. The prolonged spectral radiance in the NSP1 data as well as NIR1 and the MIR images establish that the Centaur impact

[1]Department of Geological Sciences, Brown University, Providence, RI 02912, USA. [2]NASA Ames Research Center, Moffett Field, CA 94035, USA. [3]Universities Space Research Association, Mountain View, CA 94043, USA.

*To whom correspondence should be addressed. E-mail: peter_schultz@brown.edu

Downloaded from www.sciencemag.org on May 11, 2011